

# On channel sounding with switched arrays in fast time-varying channels

Rui Wang, *Student Member, IEEE*, Olivier Renaudin, *Member, IEEE*,  
C. Umit Bas, *Student Member, IEEE*, Seun Sangodoyin, *Student Member, IEEE*,  
Andreas F. Molisch, *Fellow, IEEE*

**Abstract**—Time-division multiplexed (TDM) channel sounders, in which a single RF chain is connected sequentially via an electronic switch to different elements of an array, are widely used for the measurement of double-directional/MIMO propagation channels. This paper investigates the impact of array switching patterns on the accuracy of parameter estimation of multipath components (MPC) for a time-division multiplexed (TDM) channel sounder. The commonly-used sequential (uniform) switching pattern poses a fundamental limit on the number of antennas that a TDM channel sounder can employ in fast time-varying channels. We thus aim to design improved patterns that relax these constraints. To characterize the performance, we introduce a novel spatio-temporal ambiguity function, which can handle the non-idealities of real-world arrays. We formulate the sequence design problem as an optimization problem and propose an algorithm based on simulated annealing to obtain the optimal sequence. As a result we can extend the estimation range of Doppler shifts by eliminating ambiguities in parameter estimation. We show through Monte Carlo simulations that the root mean square errors of both direction of departure and Doppler are reduced significantly with the new switching sequence. Results are also verified with actual vehicle-to-vehicle (V2V) channel measurements.

## I. INTRODUCTION

Realistic radio channel models are essential for development and improvement of communication transceivers and protocols [1]. Realistic models in turn rely on accurate channel measurements. Various important wireless systems are operating in fast-varying channels, such as mobile millimeter wave (mmWave) [2], Vehicle-to-vehicle (V2V) [3] and high speed railway systems [4]. The need to capture the fast time variations of such channels creates new challenges for the measurement hardware as well as the signal processing techniques.

Since most modern wireless systems use multiple antennas, channel measurements also have to be done with multiple-input multiple-output (MIMO) channel sounders, also known as double-directional channel sounders. There are three types of implementation of such sounders: (i) full MIMO, where each antenna element is connected to a different RF chain [5], (ii) virtual array, where a single antenna is moved mechanically to emulate the presence of multiple antennas [6], and (iii) switched array, also known as time-division multiplexed (TDM) sounding, where different physical antenna elements are connected via an electronic switch to a single RF chain [7]. The last configuration is the most popular in particular for outdoor measurements, as it offers the best compromise between cost and measurement duration.

From measurements of MIMO impulse responses or transfer functions, it is possible to obtain the parameters (direction of departure (DoD), direction of arrival (DoA), delay, and complex amplitude) of the multipath components (MPCs) by means of High Resolution Parameter Estimation (HRPE) algorithms. Most HRPE algorithms are based on the assumption that the duration of one MIMO snapshot (the measurement of impulse responses from every transmit to every receive antenna element) is shorter than the coherence time of the channel. Equivalently, this means the MIMO cycle rate, i.e. the inverse of duration between two adjacent MIMO snapshots, should be greater than or equal to half of the maximal absolute Doppler shift, in order to avoid ambiguities in estimating Doppler shifts of MPCs. Since in a switched sounder the MIMO snapshot duration increases with the number of antenna elements, there seems to be an inherent conflict between the desire for high accuracy of the DoA and DoD estimates (which demands a larger number of antenna elements) and the admissible maximum Doppler frequency.

Yin *et al.* were the first to realize that the Doppler shift estimation range (DSER) can be extended by a factor equal to the product of transmitter (TX) and receiver (RX) antennas in TDM channel sounding [8]. They studied the problem in the context of the ISI-SAGE algorithm [9]. Pedersen *et al.* later discovered that it was the choice of sequential switching (SS) patterns that caused this limit in the TDM channel sounding [10]. Nonsequential switching (non-SS) patterns can potentially significantly extend the DSER by eliminating the ambiguities. However the analysis is performed under ideal conditions: firstly the paper assumes that all antenna elements are isotropic radiators, secondly it requires the knowledge of the phase centers of all antennas. Both assumptions are difficult to fulfill for realistic arrays used in channel sounding, given the unavoidable mutual coupling between antennas and the presence of a metallic support frame. Pedersen *et al.* proposed to use the so-called normalized sidelobe level (NSL) of the objective function as the metric to evaluate switching patterns, and further derived a necessary and sufficient condition of the switching sequences that lead to ambiguities [11], but the method to derive good switching sequences for realistic arrays is not clear. Our work attempts to close these gaps.

Our work adopts an algebraic system model that uses decompositions through effective array distribution functions (EADF) [12], which provides a reliable and elegant approach for signal processing on real-world arrays. Therefore our analysis no longer requires the isotropic radiation pattern or

prior knowledge about the antenna phase centers. Based on the Type-I ambiguity function for an arbitrary array [13], we propose a spatio-temporal ambiguity function and investigate its properties and impact on the estimation of directions and Doppler shifts of MPCs. We also demonstrate that this spatio-temporal ambiguity function is closely related to the correlation function induced from the maximum likelihood estimator (MLE) utilized in the state-of-the-art RiMAX algorithm. Inspired by Ref. [14], we model the array pattern design problem as an optimization problem and propose an annealing algorithm to search for an acceptable solution. Besides we propose an HRPE algorithm that adopts a signal data model that incorporates the optimized array switching pattern.<sup>1</sup>

The main contributions of this work are the following:

- we model the selection of array switching scheme as an optimization problem, and introduce the spatio-temporal ambiguity function that also incorporates *realistic* arrays with the aid of EADFs;
- we integrate the optimized array switching pattern into an HRPE algorithm and compare the parameter estimation variance with the Cramer-Rao lower bound (CRLB) through Monte-Carlo simulations;
- we also modify the switching pattern on a real-time MIMO channel sounder and use actual V2V measurement data to show the effectiveness of the optimized switching pattern.

The remainder of the paper is organized as follows. Section II introduces the general spatio-temporal ambiguity function and the associated signal data model used in the TDM-based channel sounding. In Section III we simplify the problem by only allowing the TX to have cycle-dependent switching patterns, and present the formulation of the optimization problem and its solution based on a simulated annealing (SA) algorithm. In Section IV we introduce an HRPE algorithm that generalizes the evaluation of TDM MIMO channel measurement and incorporates the optimized switching pattern. Section V validates the switching sequence and corresponding HRPE algorithm via extensive Monte Carlo simulations and measured V2V channel responses. In Section VI we draw the conclusions.

The symbol notation used in this paper follows the rules below.

- Bold upper case letters, such as  $\mathbf{B}$ , denote matrices. Bold lower case letters, such as  $\mathbf{b}$ , denote column vectors. For instance  $\mathbf{b}_j$  is the  $j$ -th column of the matrix  $\mathbf{B}$ .
- Calligraphic upper-case letters denote high-dimensional tensors.
- $[\mathbf{B}]_{ij}$  denotes the element in the  $i$ th row and  $j$ th column of the matrix  $\mathbf{B}$ .
- Superscripts  $\text{T}$  and  $\dagger$  denote matrix transpose and Hermitian transpose.
- The operators  $|f(\mathbf{x})|$  and  $\|\mathbf{b}\|$  denote the absolute value of a scalar-valued function  $f(\mathbf{x})$  and the Euclidean norm of a vector  $\mathbf{b}$ .

- The operators  $\otimes$ ,  $\odot$  and  $\diamond$  denote Kronecker, Schur-Hadamard, and Khatri-Rao products respectively.

## II. SIGNAL MODEL AND AMBIGUITY FUNCTION

### A. Signal Data Model

This work mainly studies the antenna switching sequence in the TDM channel sounding problem. We consider  $T$  MIMO measurement snapshots in one observation window, each with  $M_f$  frequency points,  $M_R$  receive antennas, and  $M_T$  transmit antennas. The adjacent MIMO snapshots are separated by  $T_0$ . We assume that all scatterers are placed in the far field of both TX and RX arrays, which also implies that MPCs are modeled as plane waves. Besides TX and RX arrays are vertically polarized by assumption and have frequency-independent responses within the operating bandwidth. Such  $T$  MIMO snapshots can span larger than the coherence time of the channel, but we assume that the structural parameters of the channel, also known as the large-scale parameters, such as path delay, DoA, DoD and Doppler shift, remain constant during this period.<sup>2</sup>

A *vectorized* data model for the observation of  $T$  MIMO snapshots is given in (1). It includes contributions from deterministic specular paths (SP)s  $\mathbf{s}(\boldsymbol{\theta}_{sp})$ , dense multipath components (DMC)  $\mathbf{n}_{dmc}$  and measurement noise  $\mathbf{n}_0$ .

$$\mathbf{y} = \mathbf{s}(\boldsymbol{\theta}_{sp}) + \mathbf{n}_{dmc} + \mathbf{n}_0 \quad (1)$$

The data model of an observation vector for a number of  $P$  SPs is determined by

$$\mathbf{s}(\boldsymbol{\theta}_{sp}) = \mathbf{B}(\boldsymbol{\mu}, \boldsymbol{\eta}_T, \boldsymbol{\eta}_R) \cdot \boldsymbol{\gamma}_{vv}, \quad (2)$$

where the SP parameter vector  $\boldsymbol{\theta}_{sp}$  includes the structural parameters  $\boldsymbol{\mu}$  and the path weights  $\boldsymbol{\gamma}_{vv}$ . The basis matrix  $\mathbf{B}$  has dimension  $M \times P$ , and  $M$  is the total number of observations given by  $M_f M_R M_T T$ . The  $i$ -th column stands for the vectorized basis channel vector for the  $i$ -th SP. The switching sequences  $\boldsymbol{\eta}_T$  and  $\boldsymbol{\eta}_R$  for TX and RX respectively not only affect the sequence of samples from different antennas, but also impact the phase variation because of the nature of TDM channel sounding.

The complexity of the basis matrix grows as the irregularity of switching sequence increases. Most papers assume that SS sequences are used at both TX and RX, hence the periodicity can be exploited to greatly simplify  $\mathbf{B}$ . An example of SS sequences is shown in Fig. 1. References [16] and [17] adopted a data model of SPs where the channel is assumed to be completely static within one MIMO snapshot, as a result the basis matrix is a Khatri-Rao product of three smaller matrices. To evaluate fast time-varying channel, such as the V2V communication channel, a more sophisticated signal model is used in Ref. [18], which considers the phase variation due to Doppler shifts between switched antennas, but again the model is only applicable for SS sequences.

<sup>1</sup>The conference version of this work is accepted and will be presented at IEEE International Conference on Communications 2018 [15].

<sup>2</sup>This does not mean that the channel is assumed to be static, instead for each path the phase varies over time due to the presence of Doppler shift.

## B. Spatio-temporal Ambiguity Function

The Type-I ambiguity function for an antenna array can reflect its ability to differentiate signals in the angular domain [13]. Generalizing the definition to include the full structural parameters  $\boldsymbol{\mu}$  from Eq. (2), we have a spatio-temporal ambiguity function

$$X_{tot}(\boldsymbol{\mu}, \boldsymbol{\mu}') = \frac{\mathbf{b}^\dagger(\boldsymbol{\mu})\mathbf{b}(\boldsymbol{\mu}')}{\|\mathbf{b}(\boldsymbol{\mu})\| \cdot \|\mathbf{b}(\boldsymbol{\mu}')\|}, \quad (3)$$

where  $\mathbf{b}$  is one column of the basis matrix  $\mathbf{B}$  in Eq. (2). The ambiguity function also depends on the switching sequences  $\boldsymbol{\eta}_T$  and  $\boldsymbol{\eta}_R$ , but we drop them from the notation for brevity.

More importantly this ambiguity function is closely related with the correlation function that is tightly connected with the objective function of the MLE developed in Section IV-A, hence studying the properties of this ambiguity function is critical for the performance of the MLE.

Here we introduce some properties of the ambiguity function.

**Property 1.**  $X_{tot}(\boldsymbol{\mu}, \boldsymbol{\mu}) = 1$ , and  $0 \leq |X_{tot}(\boldsymbol{\mu}, \boldsymbol{\mu}')| \leq 1$ .

It is straightforward to prove that  $X_{tot}(\boldsymbol{\mu}, \boldsymbol{\mu}) = 1$ . We can use the Cauchy-Schwartz inequality to prove the inequality  $|X_{tot}(\boldsymbol{\mu}, \boldsymbol{\mu}')| \leq 1$ , and the equality is obtained when  $\boldsymbol{\mu} = \boldsymbol{\mu}'$ .

**Property 2** (Separability of the Ambiguity Function). We can prove that the ambiguity function in Eq. (3) is a product of two component ambiguity functions of delay  $\tau$  and  $\kappa$ . The latter consists of every parameter in  $\boldsymbol{\mu}$  except  $\tau$ .

$$X_{tot}(\boldsymbol{\mu}, \boldsymbol{\mu}') = X_\tau(\tau, \tau')X(\boldsymbol{\kappa}, \boldsymbol{\kappa}') \quad (4)$$

The proof relies on the following property of Khatri-Rao products between two vectors. In fact, the Khatri-Rao product between two vectors is equivalent to the Kronecker product.

$$(\mathbf{a} \diamond \mathbf{b})^\dagger \cdot (\mathbf{a}' \diamond \mathbf{b}') = (\mathbf{a}^\dagger \mathbf{a}') \cdot (\mathbf{b}^\dagger \mathbf{b}') \quad (5)$$

This property holds when  $\mathbf{a}$  and  $\mathbf{a}'$  have the same length, so do  $\mathbf{b}$  and  $\mathbf{b}'$ . Detailed derivations are provided in Appendix A.

**Property 3.** The estimation problem has ambiguities when the following condition holds.

$$|X(\boldsymbol{\kappa}, \boldsymbol{\kappa}')| = 1, \exists \boldsymbol{\kappa}' \neq \boldsymbol{\kappa} \quad (6)$$

This spatio-temporal array ambiguity function is also closely related to the ambiguity function well studied in MIMO radar. The MIMO radar ambiguity function introduced in Ref. [14] allows TX to send different waveforms on different antennas, while our problem considers a repeated sounding waveform for all TX antennas. The Doppler-(bi)direction ambiguity function introduced in Ref. [11] is quite similar to ours. However their ambiguity function assumes that the array has identical elements without any mutual coupling effects, our ambiguity function can handle arbitrary array structures, which suits better for developing non-SS sequences for MIMO channel sounding.

## C. Simplified Signal Data Model

In this subsection we impose some constraints on the switching sequences in order to obtain a more tractable problem. As a comparison the basis matrix  $\mathbf{B}$  with the SS sequences at both TX and RX is given by [18, (20)]

$$\mathbf{B}(\boldsymbol{\mu}) = \mathbf{B}_t \diamond \tilde{\mathbf{B}}_{TV} \diamond \tilde{\mathbf{B}}_{RV} \diamond \mathbf{B}_f. \quad (7)$$

One straightforward relaxation on the switching patterns from SS sequences is to allow the TX array to have a cycle-dependent switching pattern,<sup>3</sup> hence the new basis matrix needs to merge the Khatri-Rao product of two basis matrices  $\mathbf{B}_t$  and  $\tilde{\mathbf{B}}_{TV}$  into  $\tilde{\mathbf{B}}_{TV,T}$ , in order to reflect such relaxation.

$$\mathbf{B}(\boldsymbol{\mu}) = \tilde{\mathbf{B}}_{TV,T} \diamond \tilde{\mathbf{B}}_{RV} \diamond \mathbf{B}_f \quad (8)$$

$$= \left[ \tilde{\mathbf{B}}_{TV}^1 \quad \cdots \quad \tilde{\mathbf{B}}_{TV}^T \right]^\top \diamond \tilde{\mathbf{B}}_{RV} \diamond \mathbf{B}_f, \quad (9)$$

where  $\tilde{\mathbf{B}}_{TV}^j \in \mathbb{C}^{M_T \times P}$  with  $j = 1, 2, \dots, T$  represents the spatio-temporal response of the TX array at the  $j$ -th MIMO snapshot, and  $\tilde{\mathbf{B}}_{RV} \in \mathbb{C}^{M_R \times P}$  is for the RX array with the sequential switching, and  $\mathbf{B}_f \in \mathbb{C}^{M_f \times P}$  is the basis matrix that captures the frequency response due to path delay.

Instead of allowing both TX and RX array to switch after each sounding waveform (fully-scrambled), we focus on the switching sequences where the RX first switches through all possible antennas while the TX remains connected with the same antenna. This type of sequences has a relatively simpler basis matrix compared with the fully scrambled case. Compared to (8) the fully scrambled case needs to further merge  $\tilde{\mathbf{B}}_{TV,T}$  and  $\tilde{\mathbf{B}}_{RV}$ . Another motivation for studying this type of switching sequences is the efficiency to operate the channel sounder. Many high-power TX switches tend to have a longer switching settling time than the RX switches. This type of switching sequences that we are interested in effectively limits the number of switching for the TX array, reduces the guard time needed in the sounding signal and improves the overall measurement efficiency of the channel sounder.

Since our work focuses on channel sounding in a fast time-varying channel, the phase variation within one MIMO snapshot is no longer negligible, and the new TX or RX basis matrices for the  $t$ -th MIMO snapshot become weighted versions of the static array basis matrices. The exact connections are given by

$$\tilde{\mathbf{B}}_{TV}^t = \mathbf{B}_{TV} \odot \mathbf{A}_T^t \quad (10)$$

$$\tilde{\mathbf{B}}_{RV} = \mathbf{B}_{RV} \odot \mathbf{A}_R, \quad (11)$$

where  $\mathbf{A}_R$  and  $\mathbf{A}_T^t$  are weighting matrices that capture the phase change due to effects of Doppler and switching sequences.  $\mathbf{A}_T^t$  depends on the MIMO snapshot index  $t$ , because TX implements a cycle-dependent switching pattern. Let us use a  $M_T \times T$  matrix  $\boldsymbol{\eta}_T$  to represent the TX switching pattern, the elements in the phase weighting matrices  $\mathbf{A}_T^t$  and  $\mathbf{A}_R$  are given by

$$[\mathbf{A}_T^t]_{m_T, p} = e^{j2\pi\nu_p[\boldsymbol{\eta}_T]_{m_T, t}} \quad (12)$$

$$[\mathbf{A}_R]_{m_R, p} = e^{j2\pi\nu_p m_R t_0}, \quad (13)$$

<sup>3</sup>One cycle here means one MIMO snapshot.

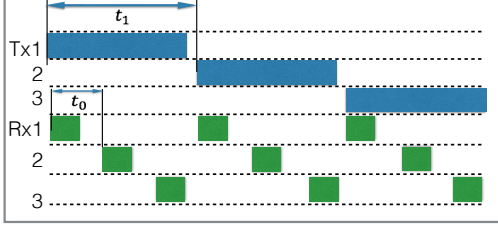


Fig. 1. An example of the SS switching for the  $3 \times 3$  MIMO setup

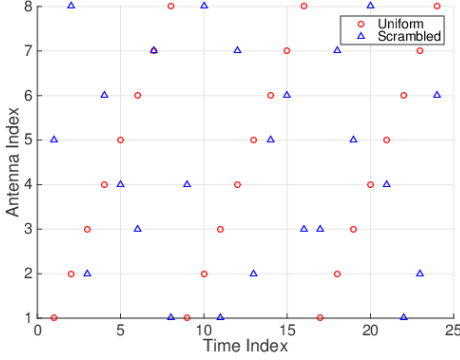


Fig. 2. Comparison between the uniform and scrambled TX switching sequences with  $M_T = 8$  and  $T = 3$

where  $\nu_p$  is the Doppler of the  $p$ -th path. As shown in the example in Fig. 1, we denote the duration between two switching events as  $t_1$  and  $t_0$  respectively for the TX and RX array. The TX switching timing matrix  $\boldsymbol{\eta}_T$  is given by

$$[\boldsymbol{\eta}_T]_{m_T, t} = (t - 1)M_T t_1 + ([\mathbf{S}_T]_{m_T, t} - 1)t_1. \quad (14)$$

$[\mathbf{S}_T]_{m_T, t}$  takes an integer value between 1 and  $M_T$  and represents the scheduled switching index of the  $m_T$ -th TX antenna for the  $t$ -th MIMO snapshot. For the SS sequence at TX, we have  $[\mathbf{S}_T]_{m_T, t} = m_T, \forall t = 1, 2, \dots, T$ . It is not difficult to see that  $\tilde{\mathbf{B}}_{TV, T}$  can be broken down into  $\mathbf{B}_t \diamond \tilde{\mathbf{B}}_{TV}$  in (7), which means the basis matrix in (9) is a generalized version of (7)

### III. SWITCHING PATTERN OPTIMIZATION

Based on Property 3, it is reasonable to argue that a good switching sequence does not lead to an estimation problem that has ambiguities. Although Ref. [11] focuses on the condition of switching sequences that generate the smallest CRLB, we have found through simulations that CRLB is almost identical for the sequential switching and the scrambled switching for practical arrays. Suppressing the sidelobe levels of the ambiguity function within the parameter domain of interest leads to better switching sequences. This is because CRLB is only relevant for unbiased estimators [19].

Instead of directly evaluating the ambiguity function in (3), we can find a *upper bound* for its amplitude, which merely

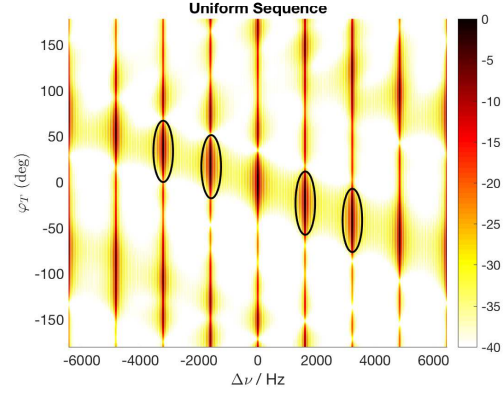


Fig. 3. Amplitude of Ambiguity function in dB with Azimuth DoD and Doppler shift, under uniform switching schemes at both Tx and Rx

depends on the azimuth DoD, the Doppler Shift, and the TX switching pattern. The upper bound is given by

$$|X_{tot}(\boldsymbol{\mu}, \boldsymbol{\mu}')| = |X_T(\tau, \tau')| \cdot |X(\boldsymbol{\kappa}, \boldsymbol{\kappa}')| \quad (15)$$

$$\leq |X(\boldsymbol{\kappa}, \boldsymbol{\kappa}')| \quad (16)$$

$$= |X_T(\varphi_T, \varphi'_T, \nu, \nu') X_R(\varphi_R, \varphi'_R, \nu, \nu')| \quad (17)$$

$$\leq |X_T(\varphi_T, \varphi'_T, \nu, \nu')|, \quad (18)$$

where the inequalities in (16) and (18) use Property 1, and Eq. (17) uses Property 2. Furthermore we find that the upper bound only depends on the Doppler difference  $\Delta\nu = \nu' - \nu$ , which is given by

$$X_T(\varphi_T, \varphi'_T, \nu, \nu') = \frac{\tilde{\mathbf{b}}_{TV, T}^\dagger(\varphi_T, \nu) \tilde{\mathbf{b}}_{TV, T}(\varphi'_T, \nu')}{\|\tilde{\mathbf{b}}_{TV, T}^\dagger(\varphi_T, \nu)\| \|\tilde{\mathbf{b}}_{TV, T}(\varphi'_T, \nu')\|} \quad (19)$$

$$= X_T(\varphi_T, \varphi'_T, \Delta\nu). \quad (20)$$

Appendix B provides a detailed derivation of Eq. (20), as well as a simpler form of  $X_T(\varphi_T, \varphi'_T, \Delta\nu)$ .

It is well known that the Doppler shifts and the impinging directions of the plane waves may contribute to phase changes at the output of the array. The Doppler shift leads to a phase rotation at the same antenna when it senses at different time instants, while the propagation direction of the plane wave also contributes to a phase change between two antennas. The *periodic* structure of the uniform switching sequence leads to ambiguities in the joint estimation of Doppler and propagation direction. It is because the estimator may find more than one plausible combination of Doppler and angle that can produce the phase changes over different antennas and time instants. For example, Fig. 3 plots the amplitude upper bound given in (18), when the TX uses the uniform switching pattern. We observe multiple peaks in addition to the central peak located at  $(0, 0)$ . It also shows that the non-ambiguous estimation range of Doppler is  $[-1/2T_0, 1/2T_0)$ , when both TX and RX implement uniform switching patterns and  $\varphi'_T = 0$ . The value of  $T_0$  in this example is  $620 \mu\text{s}$  which is based on the transmitted signal in Ref. [20].

However the design complexity for a fully scrambled switching array may become prohibitive especially when the number of antennas becomes large. Instead we resort to a

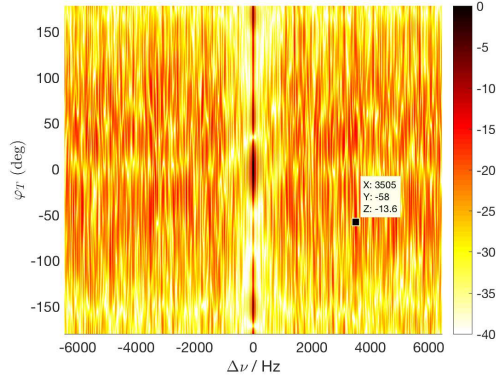


Fig. 4. Amplitude of Ambiguity function in dB with Azimuth DoD and Doppler shift, under uniform Rx switching and scrambled Tx switching scheme

simplified type of switching sequence introduced in Section II-C, where only the TX array uses a scrambled switching sequence. The DSER can potentially grow by a factor of  $M_T$  from  $1/T_0$  to  $M_T/T_0$ , compared to the maximal boost of  $M_T M_R$  in the fully scrambled case. Therefore the constraint on the switching sequence simplifies the problem formulation and the corresponding parameter extraction algorithm, while it can still provide a boost on the DSER that is sufficient for many practical purposes.

#### A. Problem Formulation

The intuitive objective of our array switching design problem is to find schemes that effectively suppress the sidelobes of the spatial-temporal ambiguity function shown in Fig. 3, hence increases the DSER. Refs. [11] and [14] prove that their ambiguity functions have constant energy, so a preferable scheme should spread the volume under the high sidelobes evenly elsewhere. However the proof again uses the idealized assumption about antenna arrays, thus it cannot be applied directly in our case. Here we introduce the function  $f_p(\boldsymbol{\eta}_T)$ , which is given by

$$f_p(\boldsymbol{\eta}_T) = \iiint_D |X_T(\varphi_T, \varphi'_T, \Delta\nu)|^p d\varphi_T d\varphi'_T d\Delta\nu, \quad (21)$$

$$D = \{(\varphi_T, \varphi'_T, \Delta\nu) | \varphi_T, \varphi'_T \in (-\pi, \pi] \& \Delta\nu \in [0, \nu_{\text{up}}]\}$$

where  $D$  is the integration intervals, and  $\nu_{\text{up}}$  represents the target maximal Doppler shift below which we want to avoid the ambiguity. This value should equal  $M_T/2T_0$ , because the periodic sequence is  $T_0/M_T$  long for the general cycle-dependent  $\boldsymbol{\eta}_T$ . Numerical simulations are conducted based on the ambiguity function in Eq. (18), with the EADF of the far-field TX array pattern calibrated in the anechoic chamber. The array is one used in a V2V MIMO channel sounder [20]. Fig. 5 suggests that the energy of the ambiguity function, i.e.  $f_2(\boldsymbol{\eta}_T)$ , is almost constant regardless of the choices of different  $\boldsymbol{\eta}_T$ . As a result we can use  $f_p(\boldsymbol{\eta}_T)$  with a higher value of  $p$  as the cost function to penalize the TX switching schemes that

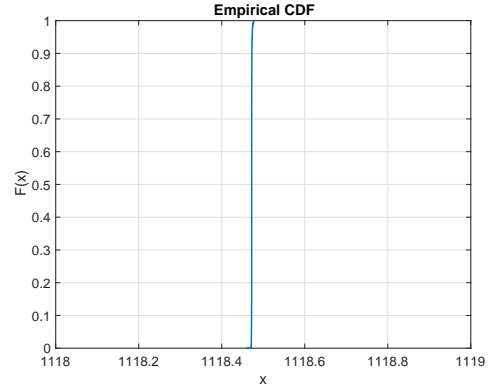


Fig. 5. The CDF of the energy of the ambiguity function with various TX switching schemes  $\boldsymbol{\eta}_T$ , based on 1000 different configurations

lead to high sidelobes. In summary our optimization problem is given by

$$\begin{aligned} \min_{\boldsymbol{\eta}_T \in \mathcal{C}} f_p(\boldsymbol{\eta}_T) \\ \text{s.t. } [\boldsymbol{\eta}_T]_{m_T, t} = ([\mathbf{S}_T]_{m_T, t} - 1)t_1 + (t - 1)M_T t_1, \end{aligned} \quad (22)$$

where the elements in the set  $\mathcal{C}$  are integer-valued matrices with a dimension of  $M_T \times T$ , and every column of  $\mathbf{S}_T$  is a permutation of the vector  $[1, 2, \dots, M_T]^T$ .

#### B. Solution and Results

Because  $\mathbf{S}_T$  takes on discrete values in the feasible set, the simulated annealing algorithm is known to solve this type of problem [21]. The pseudocode of our proposed algorithm is given here in Alg. 1. The key parameters related to this

---

**Algorithm 1** The SA-based algorithm to solve the problem (22)

---

- 1: Initialize  $\boldsymbol{\eta}_T$ , the temperature  $T = T_0$ , and  $\alpha = \alpha_0$ ;
  - 2: **while**  $k \leq k_{\text{max}}$  or  $f_p(\boldsymbol{\eta}_T) > \epsilon_{\text{th}}$  **do**
  - 3:    $\boldsymbol{\eta}'_T = \text{neighbor}(\boldsymbol{\eta}_T)$ ;
  - 4:   **if**  $\exp[(f_p(\boldsymbol{\eta}_T) - f_p(\boldsymbol{\eta}'_T))/T] > \text{random}(0, 1)$  **then**
  - 5:      $\boldsymbol{\eta}_T = \boldsymbol{\eta}'_T$
  - 6:   **end if**
  - 7:    $T = \alpha T$
  - 8: **end while**
- 

algorithm are  $p = 6$ , the initial temperature  $T_0 = 100$ , the cooling rate  $\alpha_0 = 0.97$  and the  $k_{\text{max}} = 500$ . The parameters, particularly  $\alpha_0$  and  $k_{\text{max}}$ , are selected as a tradeoff between the objective function value and the convergence speed. The operator  $\text{random}(0,1)$  outputs a random number uniformly distributed between 0 and 1. The operator  $\text{neighbor}(\boldsymbol{\eta}_T)$  provides a “neighbor” switching pattern by swapping two elements in the same column of  $\boldsymbol{\eta}_T$ .

The SA algorithm implements Markov-Chain Monte Carlo sampling on the discrete feasible set  $\mathcal{C}$ . If we denote  $f_p(\boldsymbol{\eta}_T)$  as  $e$  and  $f_p(\boldsymbol{\eta}'_T)$  as  $e'$ . The acceptance probability given by line 4 of Alg. 1 is

$$P_r(\boldsymbol{\eta}_T, \boldsymbol{\eta}'_T, T) = \begin{cases} \exp[(e - e')/T], & \text{if } e' \geq e \\ 1, & \text{otherwise} \end{cases} \quad (23)$$

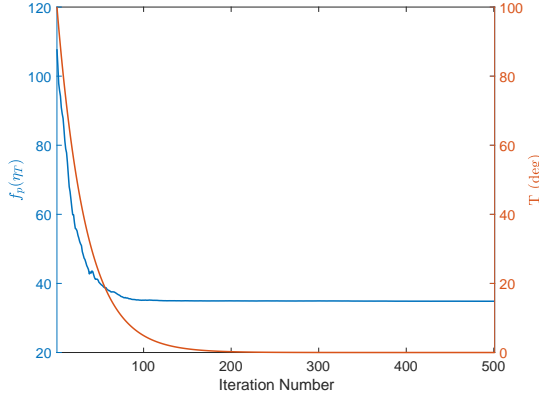


Fig. 6. The evolution of  $f_6(\eta_T)$  and temperature during the annealing algorithm in Algorithm 1

Fig. 6 provides the values of the objective function with the iteration number and decreased temperature in the SA algorithm. We present the amplitude of the 2D ambiguity function (the upper bound given in Eq. (18)) with the final switching sequence in Fig. 4, where the high sidelobes clearly disappear in contrast with Fig. 3. Another useful metric is the NSL used in Ref. [10] to measure the quality of the switching sequence. The NSL here is  $-13.60$  dB, while the lowest NSL among the three proposed sequences in Ref. [10] is  $-11.06$  dB. Given the fact that our sequence design approach is not limited to ideal uniform linear arrays and thus more flexible, the reduction of  $2.54$  dB on NSL over the best sequence in Ref. [10] is encouraging.

#### IV. PARAMETER EXTRACTION ALGORITHM

This section introduces an HRPE algorithm to evaluate the channel sounding data when the TX array employs the optimal switching sequence. It is based on the framework of RiMAX [22], which converges significantly faster than the ISI-SAGE algorithm thanks to the joint optimization of all SPs' parameters. For an introduction to the estimation framework we refer to [18, Sec. III]. We emphasize the changes made in the parameter initialization algorithm for SPs and the local optimization algorithm, when compared to our previous work [18].

##### A. Path Parameter Initialization

The outline of the parameter initialization algorithm of SPs is the same with that given in [18, Alg. 1]. It is based on the idea of subsequent signal detection, estimation and subtraction. However the main objective function used in signal detection and estimation, also known as the *correlation function*, needs to be adjusted. It is given by

$$C(\boldsymbol{\mu}, \mathbf{y}) = (\mathbf{y}^\dagger \mathbf{R}^{-1} \mathbf{B})(\mathbf{B}^\dagger \mathbf{R}^{-1} \mathbf{B})^{-1} (\mathbf{B}^\dagger \mathbf{R}^{-1} \mathbf{y}). \quad (24)$$

According to [18, Alg. 1], one important step is to evaluate the correlation function on a  $N_f \times N_R \times N_T \times N_t$  multidimensional search grid  $\tilde{\boldsymbol{\mu}}_L$ . With the increased DSER  $N_t$ , the number grid points in the time domain, requires an increase from  $2T$  to  $2M_T T$ . If we compute the correlation function given in (24)

for all possible points in  $\tilde{\boldsymbol{\mu}}_L$ , we can organize the results into a 4D tensor that shares the same dimension with  $\tilde{\boldsymbol{\mu}}_L$ . Its  $n_t$ -th child tensor in the last domain (time domain) can be expressed by

$$\mathcal{C}(:, :, :, n_t) = \mathcal{T}_1^{n_t} \odot \mathcal{T}_1^{n_t} \odot \mathcal{T}_2^{n_t}, \quad (25)$$

where  $\odot$  is the element-wise division between two tensors. Similar to our method in Ref. [17], we can exploit the data structure of  $\mathbf{B}$  and  $\tilde{\boldsymbol{\mu}}_L$ , and apply tensors products to greatly accelerate the computation [23]. Appendix D reveals the detailed procedures on how to compute the two tensors  $\mathcal{T}_1^{n_t}$  and  $\mathcal{T}_2^{n_t}$ .

##### B. Path Parameter Optimization

With an estimate of  $\mathbf{R}$  and an initial value of  $\boldsymbol{\theta}_s$ , we further improve  $\boldsymbol{\theta}_s$  with the Levenberg-Marquardt (LM) method. The update equation of  $\boldsymbol{\theta}_s$  for the  $i$ -th iteration is given by

$$\hat{\boldsymbol{\theta}}_s^{i+1} = \hat{\boldsymbol{\theta}}_s^i + [\mathcal{J}(\hat{\boldsymbol{\theta}}_s^i, \mathbf{R}) + \zeta \mathbf{I} \odot \mathcal{J}(\hat{\boldsymbol{\theta}}_s^i, \mathbf{R})]^{-1} \mathbf{q}(\mathbf{y} | \hat{\boldsymbol{\theta}}_s^i, \mathbf{R}). \quad (26)$$

This iterative optimization step requires the evaluation of the score function  $\mathbf{q}(\mathbf{y} | \boldsymbol{\theta}_s, \mathbf{R})$  and Fisher Information Matrix (FIM)  $\mathcal{J}(\boldsymbol{\theta}_s, \mathbf{R})$ . Computationally attractive methods are provided in [18, Sec. III-C]. The key to apply this method is to rewrite the Jacobian matrix  $\mathbf{D}(\boldsymbol{\theta}_s)$  as a sum of Khatri-Rao products and apply the property in (5), but an update is needed because of the new signal data model given in (2) and (9). Details about the Jacobian matrix can be found in Appendix E. The expression is given by

$$\mathbf{D}(\boldsymbol{\theta}_s) = \frac{1}{2} (\mathbf{D}_3^1 \diamond \mathbf{D}_2^1 \diamond \mathbf{D}_1 + \mathbf{D}_3^2 \diamond \mathbf{D}_2^2 \diamond \mathbf{D}_1), \quad (27)$$

where the details of each small  $\mathbf{D}$  matrix are summarized in Tab. I. To reconstruct one small  $\mathbf{D}$  matrix from this table, one can concatenate the matrices related to  $\mathbf{D}$  along the row direction. Each element in the table has  $P$  columns, where  $P$  is the number of SPs.

#### V. VALIDATION

In this section we use both Monte Carlo simulations and actual V2V measurement data to validate the choice of the switching sequence from Section III and the performance of HRPE algorithm described in Section IV, which we call RiMAX-RS for brevity. We compare it with the HRPE algorithm in Ref. [18] and will use RiMAX-4D to represent it.

##### A. Simulation

First we simulate the single-path channel, whose parameters are listed in Tab. II. To cover several cases of interest, the Doppler shift is larger than  $1/2T_0 \approx 806$  Hz in snapshot 1 and smaller than  $1/2T_0$  in snapshot 2, where  $T_0$  equals  $620 \mu\text{s}$  based on the configurations in Ref. [20]. We compare the root mean squared errors (RMSEs) with the squared root of the CRLB as a function of signal-to-noise ratio (SNR)  $\rho$  for two switching sequences, which are the SS sequence  $\eta_{T,u}$  and our optimized non-SS TX sequence  $\eta_{T,f}$ . The SNR is evaluated according to

$$\rho = \frac{\|\mathbf{s}(\boldsymbol{\theta}_s)\|^2}{\sigma_n^2} \quad (28)$$

TABLE I  
COMPONENTS TO COMPUTE THE JACOBIAN MATRIX IN (27)

	$\tau$	$\varphi_T$	$\varphi_R$	$\nu$	$\gamma_{vv,r}$	$\gamma_{vv,i}$
$\mathbf{D}_1$	$\mathbf{D}_f \diamond \gamma_{vv}^T$	$\mathbf{B}_f \diamond \gamma_{vv}^T$	$\mathbf{B}_f \diamond \gamma_{vv}^T$	$\mathbf{B}_f \diamond \gamma_{vv}^T$	$\mathbf{B}_f$	$j\mathbf{B}_f$
$\mathbf{D}_2^1$	$\tilde{\mathbf{B}}_{RV}$	$\tilde{\mathbf{B}}_{RV}$	$\mathbf{D}_{\varphi_R,V} \odot \mathbf{A}_R$	$\tilde{\mathbf{B}}_{RV}$	$\tilde{\mathbf{B}}_{RV}$	$\tilde{\mathbf{B}}_{RV}$
$\mathbf{D}_2^2$	$\tilde{\mathbf{B}}_{RV}$	$\tilde{\mathbf{B}}_{RV}$	$\mathbf{D}_{\varphi_R,V} \odot \mathbf{A}_R$	$\mathbf{B}_{RV} \odot \mathbf{D}_{\nu,R}$	$\tilde{\mathbf{B}}_{RV}$	$\tilde{\mathbf{B}}_{RV}$
$\mathbf{D}_3^1$	$\tilde{\mathbf{B}}_{TV,T}$	$\tilde{\mathbf{D}}_{\varphi_T,T}$	$\tilde{\mathbf{B}}_{TV,T}$	$2\tilde{\mathbf{D}}_{\nu,T}$	$\tilde{\mathbf{B}}_{TV,T}$	$\tilde{\mathbf{B}}_{TV,T}$
$\mathbf{D}_3^2$	$\tilde{\mathbf{B}}_{TV,T}$	$\tilde{\mathbf{D}}_{\varphi_T,T}$	$\tilde{\mathbf{B}}_{TV,T}$	$2\tilde{\mathbf{B}}_{TV,T}$	$\tilde{\mathbf{B}}_{TV,T}$	$\tilde{\mathbf{B}}_{TV,T}$

TABLE II  
PATH PARAMETERS OF ONE-PATH CHANNEL WITH HIGH DOPPLER IN SNAPSHOT 1 AND SMALL DOPPLER IN SNAPSHOT 2

Snapshot	$\tau$ (ns)	$\varphi_T$ (deg)	$\varphi_R$ (deg)	$\nu$ (Hz)
1	601.1	11.5	59.6	4032.3
2	1117.3	21.3	160.0	80.6

At each SNR value, the path weight  $\gamma$  is scaled accordingly and 1000 realizations of the channel are generated and subsequently estimated with RiMAX-RS. The theoretical CRLB can be determined based on FIM and given by

$$\sigma_{\theta_s}^2 \succeq \text{diag}(\mathcal{J}^{-1}(\theta_s)), \quad (29)$$

where  $\succeq$  is the generalized inequality for vectors. Figs. 7 and 8 provide such a comparison for  $\eta_{T,f}$ , which demonstrates its good performance in both channels with high or low Doppler. On the other hand, Fig. 9 shows the poor estimation accuracy in the high Doppler case for  $\eta_{T,u}$ , although the mean squared error (MSE) can achieve the CRLB in the low Doppler scenario as expected in Fig. 10.

We also show in Fig. 11 the delay-Doppler spectrum of snapshot 1 with three different TX switching sequences, which are  $\eta_{T,u}$ ,  $\eta_{T,d}$  (known as the “dense” sequential sequence with MIMO snapshot duration reduced to  $T_0/8$ ), and  $\eta_{T,f}$ . As a result, the spectrum in Fig. 11(a) displays multiple peaks in the same delay bin but at different Doppler shifts, while Fig. 11(c) shows that  $\eta_{T,f}$  successfully eliminates all the peaks except for one at the desired location. Notice that  $\eta_{T,f}$  also helps distribute the power under those unwanted peaks equally across Doppler. Fig. 11(b) shows that with  $\eta_{T,d}$ , we can also eliminate the repeated main peaks (and achieve slightly lower sidelobe energy); however, at the price of the separation time between adjacent MIMO snapshots is reduced to  $T_0/8$  in  $\eta_{T,w}$ , which would imply that the number of antenna elements would have to be reduced such that  $M_T M_R$  decreases by a factor of 8.

Besides we simulate a two-path channel, which is the simplest version of the multipath channel. Tab. III provides a comparison between the true and estimated parameters where we apply  $\eta_{T,f}$  and RiMAX-RS. Although both paths’ Doppler shifts are larger than  $1/2T_0$  with a small difference, the simulation suggests that the estimated parameters are close to the true values.

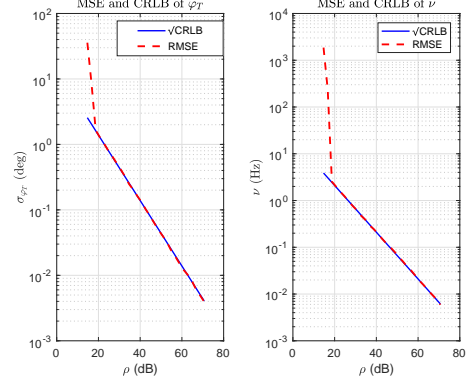


Fig. 7. Comparison about RMSEs of  $\varphi_T$  and  $\nu$  based on Monte-Carlo simulations with the theoretical CRLB from (29) for snapshot 1 in Tab. II for the optimized non-SS sequence  $\eta_{T,f}$  and RiMAX-RS

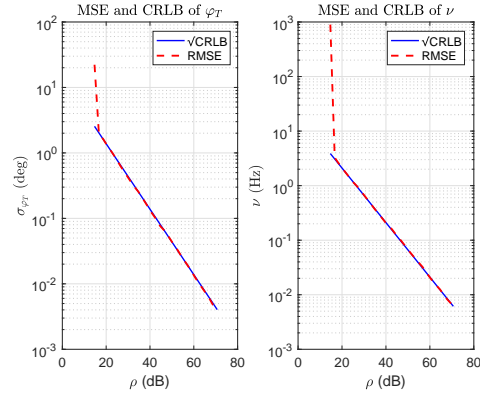


Fig. 8. Comparison about RMSEs of  $\varphi_T$  and  $\nu$  based on Monte-Carlo simulations with the theoretical CRLB from (29) for snapshot 2 in Tab. II for the optimized non-SS  $\eta_{T,f}$  and RiMAX-RS

## B. Measurement

The measurement campaign uses a real-time MIMO channel sounder developed at the University of Southern California (USC). The sounder is equipped with a pair of software defined radios (National Instruments USRP-RIO) as the main transceivers, two GPS-disciplined rubidium references as the synchronization units and a pair of 8-element uniform circular arrays (UCAs). The sounding signal is centered at 5.9 GHz with a bandwidth of 15 MHz. The maximum transmit power is 26 dBm. The main advantage of this sounder setup, compared to another V2V sounder introduced in Ref. [24], is the

TABLE III  
PARAMETER ESTIMATION FOR A TWO-PATH CHANNEL WITH  $\eta_{T,f}$ , TRUE/ESTIMATE

Path ID	$\tau$ (ns)	$\varphi_T$ (deg)	$\varphi_R$ (deg)	$\nu$ (Hz)	$ \gamma ^2$ (dB)
1	646.2/646.2	67.81/67.79	-59.33/-59.33	3225.8/3225.8	-13.13/-13.13
2	1203.7/1203.7	-60.15/-60.15	-123.79/-123.78	3217.7/3217.8	-18.82/-18.82

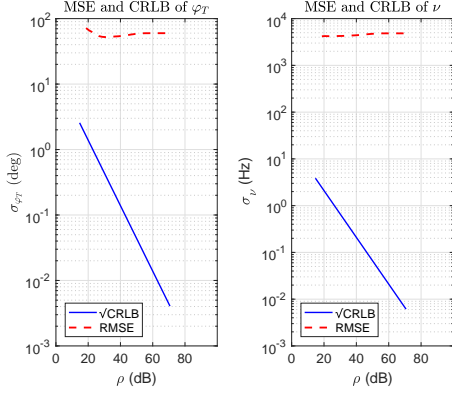


Fig. 9. Comparison about RMSEs of  $\varphi_T$  and  $\nu$  based on Monte-Carlo simulations with the theoretical CRLB from (29) for snapshot 1 in Tab. II for the SS sequence  $\eta_{T,u}$  and RiMAX-4D

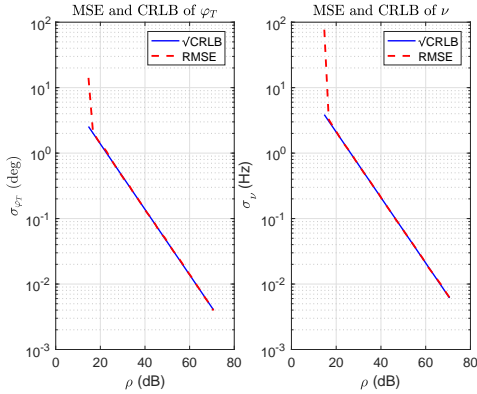


Fig. 10. Comparison about RMSEs of  $\varphi_T$  and  $\nu$  based on Monte-Carlo simulations with the theoretical CRLB from Eq. (29) for snapshot 2 in Tab. II for the SS sequence  $\eta_{T,u}$  and RiMAX-4D

fast MIMO snapshot repetition rate, which provides a more accurate representation of the channel dynamics though at the price of reduced bandwidth. More details about the sounder setup can be found in Ref. [20].

We presented first MIMO measurement results on truck-to-car (T2C) propagation channel at 5.9 GHz in Ref. [25]. The TX unit in the channel sounder was programmed to measure with switching sequences alternating between  $\eta_{T,u}$  and  $\eta_{T,f}$ . Therefore the odd MIMO burst snapshots in the data files were measured with  $\eta_{T,u}$ , while the even ones were with  $\eta_{T,f}$ . The adjacent snapshots were 50 ms apart, and it is expected that most of large scale parameters remain the same over that timescale. For the truck involved in the T2C channel measurement, we use the 5 m studio trucks as our test vehicles. Fig. 12 shows a picture of the truck and the installation of

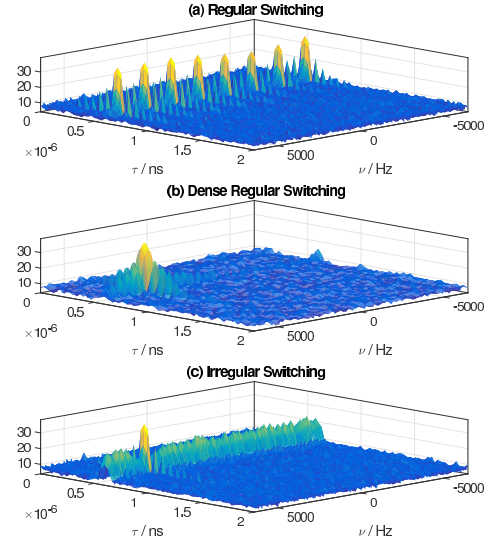


Fig. 11. Delay-Doppler spectrum of snapshot 1 with the large Doppler under different TX switching sequences, (a)  $\eta_{T,u}$  (b)  $\eta_{T,d}$  (c)  $\eta_{T,f}$

the array on top of the driving cabin. Each truck has a load capacity about 2722 kg and up to 27 m<sup>3</sup> of cargo space. The sufficient space in the driving cabin allowed us to place the equipment rack of the sounder inside. The platform that holds TX or RX antenna arrays is tightly clamped on metallic cross-bars installed on top of the driving cabin, in order to ensure the safety of the array and reduce the vibration while we drive the truck, see Fig. 12(b).



(a) The front & side view (b) Array on top of the cabin

Fig. 12. The truck used in the T2C and T2T channel measurements

To demonstrate the capability of the optimized switching sequence and the associated HRPE algorithm, we analyze several snapshots of the T2C channel measurement on I-110 North freeway near Downtown Los Angeles, California, USA. Both the truck (TX) and SUV (RX) drive in the same direction with an approximate speed of 10 m/s estimated based on the

recorded GPS locations. An incoming large truck driving in the opposite direction creates a reflected signal path associated with a large Doppler shift. Fig. 13 shows the delay and Doppler spectrum of extracted paths from RiMAX-RS, where we can observe the existence of a weak MPC with a large Doppler shift that is outside  $[-806 \text{ Hz}, 806 \text{ Hz}]$ , and it is most likely a reflection from the incoming large truck based on the delay, the large positive Doppler, and angular estimates. The incoming truck can also be observed on a video recording at a time corresponding to the snapshot. As a comparison, Fig. 14 shows the spectrum for a snapshot that is captured 50 ms ahead and processed with RiMAX-4D suitable for the SS sequence in [18]. Most of the dominant signals including the line-of-sight path and the reflection from the TX truck's trailer are present in both plots, and their Doppler shifts are around 50 Hz and delays are between 400 ns and 450 ns. However there is no component in Fig. 14 to match the MPC with large positive Doppler greater than 1 kHz in Fig. 13, instead there exists an MPC with a similar delay but a *negative* Doppler around  $-416 \text{ Hz}$ . The difference between two Doppler shifts is about 1568 Hz, which is close to  $1/T_0 \approx 1613 \text{ Hz}$  given by the length of the DSER. These experimental results also agree with our simulation results in Fig. 11 that the conventional SS sequence leads to multiple correlation peaks that are  $1/T_0$  apart.

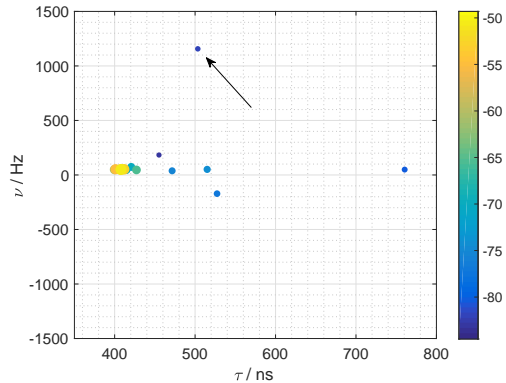


Fig. 13. The delay and Doppler spectrum at 896.45 s with each point representing a path extracted by RiMAX-RS from Sec. IV and color-coded based on the path power

## VI. CONCLUSION

In this paper we revisited the array switching design problem in the context of channel sounding for fast-time varying channels, where the popular SS sequences were shown to limit the DSER. To study the problem in the context of real-world switched arrays, we use EADFs for the array modeling which directly incorporates the array nonidealities. We analyzed specifically setups in which the TX array implements the non-SS sequence while the RX still uses the SS sequence. This design constraint reduces significantly the complexity of the HRPE algorithm and potentially increases the operation efficiency of the TDM channel sounder, while still providing a considerable boost on the DSER. Future works can pos-

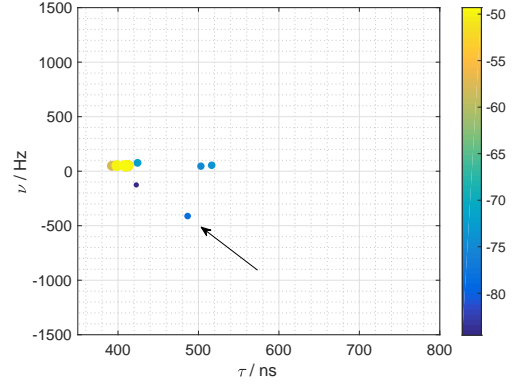


Fig. 14. The delay and Doppler spectrum at 896.40 s with each point representing a path extracted by RiMAX-4D in Ref. [18] and color-coded based on the path power

sibly look into the trade-off analysis between the operation efficiency and the increased gain on the DSER.

To find good non-SS sequences, we formulate the switching sequence design problem as an optimization problem that aims to reduce the high sidelobes in the spatio-temporal ambiguity function, and the proposed SA algorithm with carefully selected parameters can provide a non-SS sequence with a sufficiently low NSL. We integrate the switching sequence into a state-of-the-art parameter extraction algorithm. Both the switching sequence and the corresponding HRPE algorithm are verified through extensive Monte-Carlo simulations and actual sample data from T2C channel measurements on highway. This shows the capability of our design method to facilitate V2V MIMO measurements with more antennas and mm-wave MIMO measurements in dynamic environments.

## APPENDIX A DERIVATION OF SEPARABILITY OF THE AMBIGUITY FUNCTION

If we start with the basis vector based on the basis matrix in Eq. (8) and apply the property in Eq. (5) and, we can further express the inner product between two basis vectors by

$$\begin{aligned} \mathbf{b}^\dagger(\boldsymbol{\mu})\mathbf{b}(\boldsymbol{\mu}') &= [\tilde{\mathbf{b}}_{TV,T}^\dagger(\Omega_T, \nu)\tilde{\mathbf{b}}_{TV,T}(\Omega'_T, \nu')] \cdot \\ & [\tilde{\mathbf{b}}_{RV}^\dagger(\Omega_R, \nu)\tilde{\mathbf{b}}_{RV}(\Omega'_R, \nu')] \cdot \\ & [\mathbf{b}_f^\dagger(\tau)\mathbf{b}_f(\tau')], \end{aligned} \quad (30)$$

where we see that the inner product is factored into three inner products of small basis vectors from different data domains, *i.e.* frequency ( $f$ ), RX array ( $RV$ ), and TX-plus-time ( $TV, T$ ).

Similarly we can also express the denominator of the ambiguity function in Eq. (3) with vector inner products,

$$\|\mathbf{b}(\boldsymbol{\mu})\| \cdot \|\mathbf{b}(\boldsymbol{\mu}')\| = \sqrt{[\mathbf{b}^\dagger(\boldsymbol{\mu})\mathbf{b}(\boldsymbol{\mu})] \cdot [\mathbf{b}^\dagger(\boldsymbol{\mu}')\mathbf{b}(\boldsymbol{\mu}')]}, \quad (31)$$

then we can apply the separability feature derived from Eq. (30) with  $\boldsymbol{\mu}' = \boldsymbol{\mu}$  and obtain the following

$$\begin{aligned} \|\mathbf{b}(\boldsymbol{\mu})\| \cdot \|\mathbf{b}(\boldsymbol{\mu}')\| &= \|\tilde{\mathbf{b}}_{TV,T}(\Omega_T, \nu)\| \cdot \|\tilde{\mathbf{b}}_{RV}(\Omega_R, \nu)\| \cdot \\ & \|\tilde{\mathbf{b}}_{TV,T}(\Omega'_T, \nu')\| \cdot \|\tilde{\mathbf{b}}_{RV}(\Omega'_R, \nu')\| \cdot \\ & \|\mathbf{b}_f(\tau)\| \cdot \|\mathbf{b}_f(\tau')\| \end{aligned} \quad (32)$$

From Eqs. (30) and (32) we show that both the numerator and denominator in Eq. (3) can be factored into a product of two parts. The first one is only associated with delay  $\tau$ , and the other contains the rest of parameters in  $\mu$  except  $\tau$ . This means we prove that the ambiguity function is a product of two component ambiguity functions, which is given in Eq. (4).

## APPENDIX B A SIMPLER EXPRESSION OF $X_T$

In this appendix we provide a simpler expression of the essential ambiguity function  $X_T(\varphi_T, \varphi'_T, \nu, \nu')$  given by Eq. (20). This simplification is made possible by exploiting the structure of  $\mathbf{b}_{TV,T}$ , when TX implements a cycle-dependent switching pattern and RX uses a sequential switching pattern.

The derivation of Eq. (20) requires another property related with the Hadamard-schur product of two column vectors. It is given by

$$(\mathbf{a}_1 \odot \mathbf{b}_1)^\dagger (\mathbf{a}_2 \odot \mathbf{b}_2) = (\mathbf{a}_1 \odot \mathbf{a}_2^*)^\dagger (\mathbf{b}_1^* \odot \mathbf{b}_2), \quad (33)$$

where  $\mathbf{a}_1$ ,  $\mathbf{a}_2$ ,  $\mathbf{b}_1$  and  $\mathbf{b}_2$  have the same length. Using this property we can express the numerator of Eq. (19) by

$$\begin{aligned} & \sum_{t=1}^T \tilde{\mathbf{b}}_{TV,T}^t(\varphi_T, \nu)^\dagger \tilde{\mathbf{b}}_{TV,T}^t(\varphi'_T, \nu') \\ &= \sum_{t=1}^T [\mathbf{b}_{TV}(\varphi_T) \odot e^{j2\pi\nu\eta_T^t}]^\dagger [\mathbf{b}_{TV}(\varphi'_T) \odot e^{j2\pi\nu'\eta_T^t}] \\ &= \left[ \mathbf{b}_{TV}(\varphi_T) \odot \mathbf{b}_{TV}^*(\varphi'_T) \right]^\dagger \sum_{t=1}^T e^{j2\pi(\nu'-\nu)\eta_T^t} \end{aligned} \quad (34)$$

Besides the Euclidean norm in the denominator of Eq. (19) can be efficiently evaluated by substituting  $\varphi'_T$  with  $\varphi$  and  $\nu'$  with  $\nu$ .

$$\begin{aligned} \|\tilde{\mathbf{b}}_{TV,T}(\varphi_T, \nu)\| &= \sqrt{\tilde{\mathbf{b}}_{TV,T}(\varphi_T, \nu)^\dagger \tilde{\mathbf{b}}_{TV,T}(\varphi_T, \nu)} \\ &= \sqrt{T} \cdot \|\mathbf{b}_{TV}(\varphi_T)\| \end{aligned} \quad (35)$$

## APPENDIX C AMBIGUITY FUNCTION AND CORRELATION FUNCTION

This appendix provides the relationship between the ambiguity function  $X_{tot}$  and the correlation function  $C(\mu, \mathbf{y})$  in Eq. (24). Assuming there is one SP, we replace  $\mathbf{B}$  with  $\mathbf{b}$  in the derivation. Furthermore with large SNR the observation vector  $\mathbf{y}$  can be replaced by its mean or  $\mathbf{b}(\mu')\gamma_{vv}$ . Finally we also assume that  $\mathbf{R} = \sigma_n^2 \mathbf{I}$ . After incorporating three assumptions we have

$$\begin{aligned} C(\mu, \mathbf{y}(\mu')) &= \frac{1}{\sigma_n^2} (\mathbf{y}^\dagger \mathbf{b})(\mathbf{b}^\dagger \mathbf{b})^{-1} (\mathbf{b}^\dagger \mathbf{y}) \\ &= \frac{1}{\sigma_n^2} \frac{[\mathbf{b}^\dagger(\mu') \mathbf{b}(\mu) \gamma_{vv}^*] [\mathbf{b}^\dagger(\mu) \mathbf{b}(\mu') \gamma_{vv}]}{\mathbf{b}^\dagger(\mu) \mathbf{b}(\mu)} \\ &= \frac{|\gamma_{vv}|^2 |\mathbf{b}^\dagger(\mu) \mathbf{b}(\mu')|^2}{\sigma_n^2 \|\mathbf{b}(\mu)\|^2} \\ &\approx \rho_{vv} \frac{|\mathbf{b}^\dagger(\mu) \mathbf{b}(\mu')|^2}{\|\mathbf{b}(\mu)\| \cdot \|\mathbf{b}(\mu')\|} \\ &= \rho_{vv} |X_{tot}|^2, \end{aligned} \quad (36)$$

where the approximation assumes that  $\|\mathbf{b}(\mu)\|$  has similar values for different  $\mu$ . This is more or less fulfilled for antenna arrays such as UCA designed to cover signals from all possible azimuth angles.

The derivation in Eq. (36) shows that our proposed ambiguity function is closely related with the correlation function and hence the MLE developed in Sect. IV.

## APPENDIX D COMPUTATION OF 3D TENSORS $\mathcal{T}_1$ AND $\mathcal{T}_2$

Similar to the parameter initialization method in [18, Appendix A], we first construct a 4D tensor  $\mathcal{Y}'$  from  $\mathbf{y}$ , then reorganize it by combining the data in the last two dimensions, i.e. TX array and time, into one dimension.

$$\mathcal{Y}'_{3D} = \text{reshape}(\mathcal{Y}', [M_f \ M_R \ M_T T]), \quad (37)$$

where reshape() is a standard MATLAB function. The dimension of the 3D tensor  $\mathcal{Y}'_{3D}$  is  $M_f \times M_R \times M_T T$ . As a result we can compute  $\mathcal{T}_1^{n_t}$  as

$$\mathcal{T}_1^{n_t} = [(\mathcal{Y}'_{3D} \times_1 \mathbf{B}_f^\dagger) \times_2 \mathbf{B}_{RV}^{n_t \dagger}] \times_3 \mathbf{B}_{TV,T}^{n_t \dagger}. \quad (38)$$

The expressions of  $\mathbf{B}_f^\dagger$  and  $\mathbf{B}_{RV}^{n_t \dagger}$  can be readily found in [18, (61-62)], while  $\mathbf{B}_{TV,T}^{n_t \dagger}$  is a new component and given as follows.

$$\mathbf{B}_{TV,T}^{n_t \dagger} = (\mathbf{U}_t \otimes \mathbf{U}_T)^\dagger (\mathbf{B}_{TV,T} \odot \mathbf{A}_{t,N_T}(\nu_{n_t})), \quad (39)$$

where  $\mathbf{B}_{TV,T} \in \mathbb{C}^{M_T T \times N_T}$  is vertically stacked with  $T$  copies of  $\mathbf{B}_{TV}$ , and the matrix-valued function  $\mathbf{A}_{t,N_T}(\nu_{n_t}) \in \mathbb{C}^{M_T T \times N_T}$  is constructed by horizontally stacking  $N_T$  copies of the column vector  $\mathbf{a}_T(\nu_{n_t})$ . This column vector is built by concatenating the columns of  $\mathbf{A}_T^t$  with  $t = 1, 2, \dots, T$ , which are related with the  $n_t$ -th grid point of Doppler shift and given in (12).

For another key element  $\mathcal{T}_2^{n_t}$  used in Eq. (25), we again can follow the method outlined in [18, Appendix A] with some minor adjustments. First we need to build a 3D tensor  $\mathcal{L}_i$  based on the eigenvalues of  $\mathbf{R}$ , which is given by

$$\mathcal{L}_i = \text{reshape}(\text{diag}(\boldsymbol{\Lambda}^{-1}, [M_f \ M_R \ M_T T])). \quad (40)$$

Then the child-tensor  $\mathcal{T}_2^{n_t}$  can be computed with tensor products according to

$$\mathcal{T}_2^{n_t} = [(\mathcal{L}_i \times_1 (\mathbf{B}\mathbf{B}_f')^T) \times_2 (\mathbf{B}\mathbf{B}_{RV}^{n_t})^T] \times_3 (\mathbf{B}\mathbf{B}_{TV,T}^{n_t})^T. \quad (41)$$

## APPENDIX E JACOBIAN MATRIX $\mathbf{D}(\boldsymbol{\theta}_s)$

The Jacobian matrix  $\mathbf{D}(\boldsymbol{\theta}_s)$  is defined as

$$\mathbf{D}(\boldsymbol{\theta}_s) = \frac{\partial}{\partial \boldsymbol{\theta}_s^T} \mathbf{s}(\boldsymbol{\theta}_s), \quad (42)$$

with each column related to one partial derivative. More details about different columns in  $\mathbf{D}(\boldsymbol{\theta}_s)$  are given by

$$\frac{\partial}{\partial \boldsymbol{\tau}^T} \mathbf{s}(\boldsymbol{\theta}_{sp}) = \tilde{\mathbf{B}}_{TV,T} \diamond \tilde{\mathbf{B}}_{RV} \diamond \mathbf{D}_f \diamond \boldsymbol{\gamma}_{vv}^T \quad (43)$$

$$\frac{\partial}{\partial \boldsymbol{\varphi}_T^T} \mathbf{s}(\boldsymbol{\theta}_{sp}) = \begin{bmatrix} \mathbf{D}_{\varphi_T,V} \odot \mathbf{A}_T^1 \\ \vdots \\ \mathbf{D}_{\varphi_T,V} \odot \mathbf{A}_T^T \end{bmatrix} \diamond \tilde{\mathbf{B}}_{RV} \diamond \mathbf{B}_f \diamond \boldsymbol{\gamma}_{vv}^T \quad (44)$$

$$\frac{\partial}{\partial \boldsymbol{\varphi}_R^T} \mathbf{s}(\boldsymbol{\theta}_{sp}) = \tilde{\mathbf{B}}_{TV,T} \diamond (\mathbf{D}_{\varphi_R,V} \odot \mathbf{A}_R) \diamond \mathbf{B}_f \diamond \boldsymbol{\gamma}_{vv}^T \quad (45)$$

$$\frac{\partial}{\partial \boldsymbol{\gamma}_{vv,r}^T} \mathbf{s}(\boldsymbol{\theta}_{sp}) = \tilde{\mathbf{B}}_{TV,T} \diamond \tilde{\mathbf{B}}_{RV} \diamond \mathbf{B}_f \quad (46)$$

$$\frac{\partial}{\partial \boldsymbol{\gamma}_{vv,i}^T} \mathbf{s}(\boldsymbol{\theta}_{sp}) = j \tilde{\mathbf{B}}_{TV,T} \diamond \tilde{\mathbf{B}}_{RV} \diamond \mathbf{B}_f, \quad (47)$$

where  $j$  stands for the unit imaginary number here. Particularly the partial derivative with respect to the Doppler shift is determined by

$$\frac{\partial}{\partial \boldsymbol{\nu}^T} \mathbf{s}(\boldsymbol{\theta}) = \begin{bmatrix} \mathbf{B}_{TV} \odot \mathbf{D}_T^1 \\ \cdots \\ \mathbf{B}_{TV} \odot \mathbf{D}_T^t \\ \cdots \\ \mathbf{B}_{TV} \odot \mathbf{D}_T^T \end{bmatrix} \diamond \tilde{\mathbf{B}}_{RV} \diamond \mathbf{B}_f \diamond \boldsymbol{\gamma}_{vv}^T + \tilde{\mathbf{B}}_{TV,T} \diamond (\mathbf{B}_{RV} \odot \mathbf{D}_{\nu,R}) \diamond \mathbf{B}_f \diamond \boldsymbol{\gamma}_{vv}^T. \quad (48)$$

Most of the  $\mathbf{D}$  matrices in this appendix and Tab. I are given in [18, (78)-(83)] except for  $\mathbf{D}_T^j$  with  $j = 1, 2, \dots, T$ , which is determined by  $\mathbf{D}_T^j = \mathcal{D}(\mathbf{A}_T^j, \boldsymbol{\nu})$ . The operator  $\mathcal{D}()$  is defined based on [18, (77)].

## REFERENCES

- [1] A. F. Molisch, *Wireless Communications*, 2nd ed. IEEE Press - Wiley, 2011.
- [2] S. Hur and et al., "Feasibility of mobility for millimeter-wave systems based on channel measurement," *IEEE Communications Magazine*, submitted.
- [3] C. F. Mecklenbrauker, A. F. Molisch, J. Karedal, F. Tufvesson, A. Paier, L. Bernadó, T. Zemen, O. Klemp, and N. Czink, "Vehicular channel characterization and its implications for wireless system design and performance," *Proceedings of the IEEE*, vol. 99, no. 7, pp. 1189–1212, 2011.
- [4] C.-X. Wang, A. Ghazal, B. Ai, Y. Liu, and P. Fan, "Channel measurements and models for high-speed train communication systems: a survey," *IEEE communications surveys & tutorials*, vol. 18, no. 2, pp. 974–987, 2016.
- [5] M. Kim, J.-i. Takada, Y. Chang, J. Shen, and Y. Oda, "Large scale characteristics of urban cellular wideband channels at 11 GHz," in *Antennas and Propagation (EuCAP), 2015 9th European Conference on*. IEEE, 2015, pp. 1–4.
- [6] U. Martin, "Spatio-temporal radio channel characteristics in urban macrocells," *IEE Proceedings-Radar, Sonar and Navigation*, vol. 145, no. 1, pp. 42–49, 1998.
- [7] R. S. Thoma, D. Hampicke, A. Richter, G. Sommerkorn, A. Schneider, U. Trautwein, and W. Wirmitzer, "Identification of time-variant directional mobile radio channels," *IEEE Transactions on Instrumentation and Measurement*, vol. 49, no. 2, pp. 357–364, 2000.
- [8] X. Yin, B. H. Fleury, P. Jourdan, and A. Stucki, "Doppler frequency estimation for channel sounding using switched multiple-element transmit and receive antennas," in *Global Telecommunications Conference, 2003. GLOBECOM'03. IEEE*, vol. 4. IEEE, 2003, pp. 2177–2181.
- [9] B. H. Fleury, X. Yin, P. Jourdan, and A. Stucki, "High-resolution channel parameter estimation for communication systems equipped with antenna arrays," in *Proc. 13th Ifac Symposium on System Identification (sysid 2003)*, 2003.
- [10] T. Pedersen, C. Pedersen, X. Yin, B. H. Fleury, R. R. Pedersen, B. Bozinovska, A. Hviid, P. Jourdan, and A. Stucki, "Joint estimation of Doppler frequency and directions in channel sounding using switched Tx and Rx arrays," in *Global Telecommunications Conference, 2004. GLOBECOM'04. IEEE*, vol. 4. IEEE, 2004, pp. 2354–2360.
- [11] T. Pedersen, C. Pedersen, X. Yin, and B. H. Fleury, "Optimization of spatiotemporal apertures in channel sounding," *Signal Processing, IEEE Transactions on*, vol. 56, no. 10, pp. 4810–4824, 2008.
- [12] F. Belloni, A. Richter, and V. Koivunen, "Doa estimation via manifold separation for arbitrary array structures," *IEEE Transactions on Signal Processing*, vol. 55, no. 10, pp. 4800–4810, 2007.
- [13] M. Erić, A. Zejak, and M. Obradović, "Ambiguity characterization of arbitrary antenna array: Type I ambiguity," in *Spread Spectrum Techniques and Applications, 1998. Proceedings., 1998 IEEE 5th International Symposium on*, vol. 2. IEEE, 1998, pp. 399–403.
- [14] C.-Y. Chen and P. Vaidyanathan, "MIMO radar ambiguity properties and optimization using frequency-hopping waveforms," *Signal Processing, IEEE Transactions on*, vol. 56, no. 12, pp. 5926–5936, 2008.
- [15] R. Wang, O. Renaudin, C. U. Bas, S. Sangodoyin, and A. F. Molisch, "Antenna switching sequence design for channel sounding in a fast time-varying channel," in *Communications (ICC), IEEE International Conference on*. IEEE, 2018 (accepted).
- [16] J. Salmi, A. Richter, and V. Koivunen, "Detection and tracking of MIMO propagation path parameters using state-space approach," *Signal Processing, IEEE Transactions on*, vol. 57, no. 4, pp. 1538–1550, 2009.
- [17] R. Wang, O. Renaudin, R. M. Bernas, and A. F. Molisch, "Efficiency improvement for path detection and tracking algorithm in a time-varying channel," in *Vehicular Technology Conference (VTC fall), 2015 IEEE 82nd*. IEEE, 2015.
- [18] R. Wang, O. Renaudin, C. U. Bas, S. Sangodoyin, and A. F. Molisch, "High-resolution parameter estimation for time-varying double directional V2V channel," *IEEE Transactions on Wireless Communications*, vol. 16, no. 11, pp. 7264–7275, 2017.
- [19] S. M. Kay, "Fundamentals of statistical signal processing, volume i: Estimation theory (v. 1)," *PTR Prentice-Hall, Englewood Cliffs*, 1993.
- [20] R. Wang, C. U. Bas, O. Renaudin, S. Sangodoyin, U. T. Virk, and A. F. Molisch, "A real-time MIMO channel sounder for vehicle-to-vehicle propagation channel at 5.9 GHz," in *Communications (ICC), 2017 IEEE International Conference on*. IEEE, 2017, pp. 1–6.
- [21] S. Kirkpatrick, C. D. Gelatt, M. P. Vecchi *et al.*, "Optimization by simulated annealing," *science*, vol. 220, no. 4598, pp. 671–680, 1983.
- [22] A. Richter, "Estimation of radio channel parameters: Models and algorithms," Ph.D. dissertation, Techn. Univ. Ilmenau, Ilmenau, Germany, May 2005. [Online]. Available: <http://www.db-thueringen.de>.
- [23] B. W. Bader, T. G. Kolda *et al.*, "MATLAB tensor toolbox version 2.5," Available online, January 2012. [Online]. Available: <http://www.sandia.gov/tgkolda/TensorToolbox/>
- [24] T. Abbas, J. Karedal, F. Tufvesson, A. Paier, L. Bernadó, and A. F. Molisch, "Directional analysis of vehicle-to-vehicle propagation channels," in *Vehicular Technology Conference (VTC Spring), 2011 IEEE 73rd*. IEEE, 2011, pp. 1–5.
- [25] R. Wang, O. Renaudin, C. U. Bas, S. Sangodoyin, and A. F. Molisch, "Vehicle-to-vehicle propagation channel for truck-to-truck and mixed passenger freight convoy," in *Personal, Indoor, and Mobile Radio Communications (PIMRC), 2017 IEEE 28th Annual International Symposium on*. IEEE, 2017, pp. 1–5.